Journal of Applied Physics

Morphology induced spectral reflectance lineshapes in VO_2 thin films

Cite as: J. Appl. Phys. **125**, 223103 (2019); https://doi.org/10.1063/1.5086272
Submitted: 19 December 2018 . Accepted: 19 May 2019 . Published Online: 13 June 2019

Merve Ertas Uslu, Refet Ali Yalcin, I. Burc Misirlioglu, and Kursat Sendur

AIP Publishing

Journal of Applied Physics ARTICLE scitation.org/journal/jap

Morphology induced spectral reflectance lineshapes in VO_2 thin films

Cite as: J. Appl. Phys. **125**, 223103 (2019); doi: 10.1063/1.5086272
Submitted: 19 December 2018 · Accepted: 19 May 2019 ·
Published Online: 13 June 2019

Merve Ertas Uslu,[1,2] Refet Ali Yalcin,[1] I. Burc Misirlioglu,[1,2,3,a)] and Kursat Sendur[1,2,b)]

AFFILIATIONS

[1]Faculty of Engineering and Natural Sciences, Sabanci University, Orhanli/Tuzla 34956, Istanbul, Turkey
[2]Sabanci University Nanotechnology Application Center, Orhanli/Tuzla 34956, Istanbul, Turkey
[3]Integrated Manufacturing Technologies Research and Application Center, Sabanci University, Tuzla 34956, Istanbul, Turkey

[a)]burc@sabanciuniv.edu
[b)]sendur@sabanciuniv.edu

ABSTRACT

In this work, we study the spectral reflectance of VO_2 thin films and identify the specific contributions of the morphology and phase transition to optical spectra. The formation of highly [011] textured VO_2 thin films on Si was achieved by an oxidation process starting with a metallic V thin film grown on an [001] Si substrate by an evaporation technique. Structural (XRD and Raman) and spectroscopic (XPS) characterization results indicate high purity VO_2 formation with different sizes at various annealing temperatures without any change in the composition. Temperature dependent spectral reflectance distributions reveal that the insulator-to-metal transition (IMT) phase transition temperature of the VO_2 nanostructures shows a slight size-dependence (~3 °C), but this feature can be overshadowed by morphology that can lead to the misinterpretation of transition characteristics. The spectral line shape of the reflectance curves in the visible and near-infrared regions show substantially different characteristics for the samples annealed at different temperatures. Using numerical scattering calculations, we conclude that the changes in the optical response can be explained by morphological effects instead of changes in the intrinsic material properties such as a shift in the IMT temperature. Furthermore, the main mechanism leading to different spectral line shapes is the morphological differences leading to diffuse and specular reflectance.

I. INTRODUCTION

Insulator-to-metal transition (IMT) of VO_2 has recently attracted great attention for a variety of applications including electronic switches and thermal management.[1–4] During heating, bulk VO_2 changes from a monoclinic to a tetragonal structure accompanied by an IMT at a critical temperature (T_C) of 68 °C.[5,6] The metallic state of VO_2 reflects the infrared region of the electromagnetic spectrum above T_C. Due to this property of VO_2, several studies have been centered around the growth of this material in a thin film form[7–21] due to its potential applications in smart optoelectronic devices,[22–26] chemical and biochemical sensors,[27,28] and thermal management purposes.[29–32]

The size dependence of IMT in VO_2 has been studied akin to other systems displaying phase change and with the potential for use as functional components.[33,34] Nanocrystalline forms can exhibit physical characteristics different from that of bulk VO_2 that can impact the thermodynamically stable crystal state as well as the electronic band structure. A number of works have reported variations in the reflectance and the resistivity of these materials as a function of grain size or film thickness.[35–39] When it comes to the optical response of such deposits, both the electronic state of VO_2 and also the collective response of the constituent grains become important. Apart from phase transition-related changes in the optical response of a surface, it is well known that the shape, diameter, and aerial density of the structures formed on a surface affect light scattering characteristics, and hence surface reflectivity. Therefore, the ability to distinguish the intrinsic material property effects from geometrical ones during light scattering becomes a crucial parameter in understanding and tailoring the optical response of such structures.

In this work, we demonstrate size driven changes in the spectral reflectance of VO_2 thin films on Si substrates. We employed an e-beam evaporation technique to grow metallic amorphous V films followed by the annealing of these deposits at different temperatures

to enable us to acquire dense and coarse (250–300 nm) and fine sized (100–150 nm) VO_2 thin films. Temperature dependent ellipsometry analyses indicate that the IMT phase transition temperature of VO_2 thin films shows a grain size-dependence. In addition, the oscillatory spectral reflectance line shapes are observed in the visible regime in fine grain structures. The striking variation in the reflectance in the visible regime upon the change in the grain size of VO_2 deposits tempts one to associate it with the lowering of the IMT in fine grained samples. Carrying out numerical simulations on electromagnetic wave scattering from nanofeatured surfaces resembling the VO_2 samples here, however, we identify that this behavior is emanating solely from geometrical scattering effects rather than a size dependence of the intrinsic material properties, a point overlooked in the literature. For the coarser grained samples obtained via annealing at higher temperatures, spectral line shapes are almost flat in the visible regime independent of temperature, again in agreement with our numerical calculations.

II. MATERIALS AND METHODS

A. Experimental techniques

To fabricate the VO_2 nanocrystalline films, we followed the technique reported in our recent work.[40] A metallic V thin film layer was grown on an [001] Si substrate by the e-beam evaporation technique under a base pressure better than 3×10^{-6} Torr as shown in Fig. 1(a). The growth pressure during the process was maintained at 6.9×10^{-6} Torr. Prior to deposition, the [001] Si substrate was ultrasonically cleaned in acetone and isopropyl alcohol to remove all contamination, followed by a drying process via nitrogen gas. V thin film coating was deposited at room temperature with a deposition rate of 0.5 Å/s, where high purity V (99.9%) metal was used as a target placed in a W crucible. The deposition was initially made on a 4-in. Si wafer after which the V coated wafer was dissected into smaller pieces for further processing as presented in Fig. 1(c). Following this step, we carried out a heat treatment on three different samples for 2 h at 400 °C, 500 °C, and 600 °C, as schematically shown in Fig. 1(d) under controlled Ar gas (purity 99.8%) at a fixed flow rate of 2 l/min to obtain VO_2 nanocrystalline deposits with varying grain sizes, which are illustrated in Figs. 1(e), 1(f), and 2.

The crystal structure and growth orientation of the prepared samples were characterized by X-ray diffraction (XRD) under Cu Kα radiation (1.5418 Å) in the 2θ range varying from 20° and 80° using a Bruker diffractometer. Raman scattering spectroscopy was used to confirm the VO_2 phase at room temperature using a Renishaw inVia Reflex Raman Spectroscopy with a 532 nm laser beam in the range of 110–990 cm^{-1}. The laser was focused on the sample with a 50× objective. Surface morphology and grain size distribution of the prepared samples were analyzed with a scanning electron microscopy (SEM) instrument at an accelerating voltage of 5 kV (Model FEG-SEM Leo Supra 35 and Bruker Flash). As trace amounts (<1.5%–2%) of oxides of V other than VO_2 might go undetected in XRD, we also checked the sample composition with X-ray photoemission spectroscopy (XPS) (Thermo Scientific K-Alpha X-ray) equipped with an aluminum anode (Al Kα = 1468.3 eV) at a 90° electron takeoff angle (between the film surface and the axis of the analyzer lens). Pass energy of 50 eV and an energy step of 0.1 eV were set to acquire the data. Spectra were recorded and processed using the Avantage 5.9 software. Spectral reflectance measurements were performed with a WASE 400 ellipsometry as a function of temperature for unpolarized light incident at 30° in the wavelength range of 300–2100 nm allowing us to probe the near UV and far IR frequency of our samples at various temperatures as illustrated in Figs. 1(g) and 1(h). We used ellipsometry measurements to detect the IMT temperatures of our samples.

B. Theoretical and numerical techniques

To shed light on the experimental results, we carried out numerical simulations for spectral reflectance of the VO_2 nanocrystalline surface. For this purpose, we computed the bidirectional reflectance of VO_2 films using different techniques in the literature depending on the wavelength/size ratio. In the literature, the estimation of bidirectional reflectance of closely packed grain layers has been studied, and predictions from numerical models were compared with the experimental data.[41]

For small particles ($r/\lambda < 0.1$), the bidirectional reflectance of the coating is calculated with the Fresnel formalism, where the refractive index of the medium is estimated with the effective medium theory (EMT). The Lewis–Nielsen method[42] is used to estimate effective medium properties in this study. When the particle size is small compared to the wavelength ($r/\lambda < 0.1$), the mixture in which particles are dispersed in the matrix behaves like a homogenous material. The dielectric function of this resulting mixture is calculated using the Lewis–Nielsen method,

$$\frac{\epsilon}{\epsilon_m} = \frac{1 + ABf_v}{1 - B\varphi f_v}, \tag{1}$$

$$A = \frac{1}{A_e} - 1, \tag{2}$$

$$\mathrm{B} = \frac{\epsilon_p/\epsilon_m - 1}{\epsilon_p/\epsilon_m + A}, \tag{3}$$

$$\varphi = 1 + \frac{1 - f_{max}}{f_{max}^{\,2}} f_v, \tag{4}$$

where ϵ, ϵ_p, and ϵ_m are dielectric functions of mixture, grain, and matrix, respectively, f_{max} is the maximum packing fraction that is 0.637 for random close pack,[42] A_e is the depolarization factor that is 0.4 for spheres.[42] The technique summarized above was used in computing the bidirectional reflectance of the fine sized VO_2 grains obtained at 500 °C annealing.

For particles having sizes comparable to the incident wavelength ($r/\lambda > 0.1$), scattering is no longer negligible, and the estimations of EMT deviate from the exact solution as the scattering effects become more dominant.[41] To solve the spectral reflectance of a surface composed of densely coated large particles, full-wave solutions of wave optics are used.[43] The discrete dipole approximation (DDA), also known as the coupled dipole approximation, is used to model the reflectance of a coating with large particles having sizes comparable to the wavelength of the incident radiation. Due to its ability to handle periodic and random shaped structures,

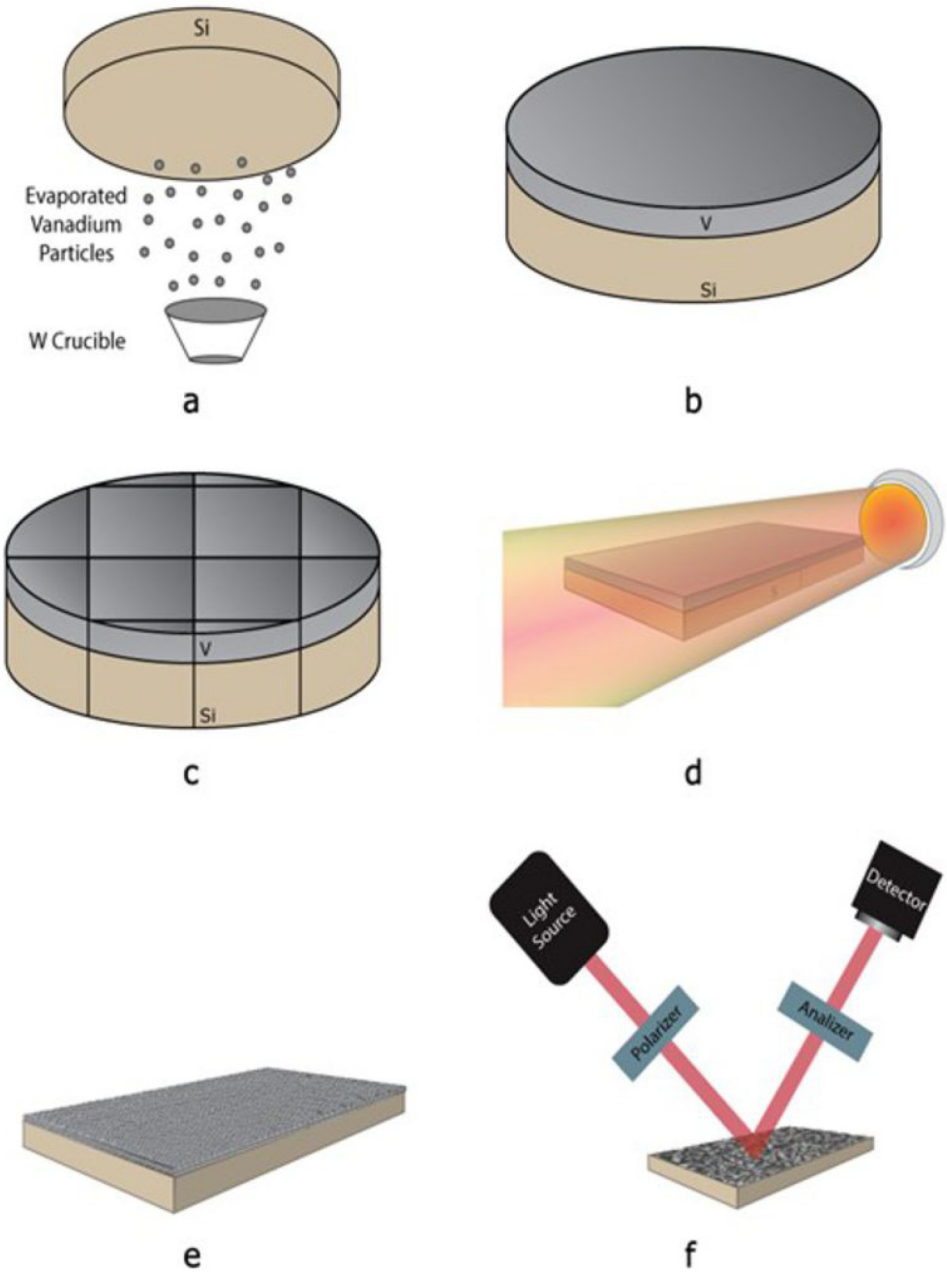

FIG. 1. (a) A metallic V thin film layer is grown on an Si substrate by e-beam evaporation, (b) the resulting coating is shown. (c) V coated wafer was dissected into smaller pieces for further processing. (d) Heat treatment on three different samples for 2 h at 400, 500, and 600 °C in a tube furnace. VO_2 nanocrystalline deposits with varying grain size depending on the temperature as shown in (e) and (f). Bidirectional reflectance of the coating was measured using ellipsometry.

DDA is used to estimate optical properties of the coating where the grain size is comparable to the wavelength. The DDA was first proposed by Purcell and Pennypacker.[44] The periodic structure implementation of the DDA with the calculation of reflectance, transmittance, and absorptance was developed by Draine and Flatau.[45,46] In the DDA technique, geometry is modeled with polarizable points with specified polarizabilities. The formulation of DDA is a well-established technique in the literature[44] and will not be repeated here. Open source discrete dipole scattering (DDSCAT) is used as the DDA solver, which was reported to have a higher accuracy compared to other versions.[47] In this study, the spectral reflectance of coarse grain sized VO_2 specimens was studied using the DDA method. Incident radiation is introduced as an unpolarized plane wave with a polar angle matched to the ellipsometry data. In the calculations, the refractive index and optical loss constant of VO_2 were taken from the literature.[48]

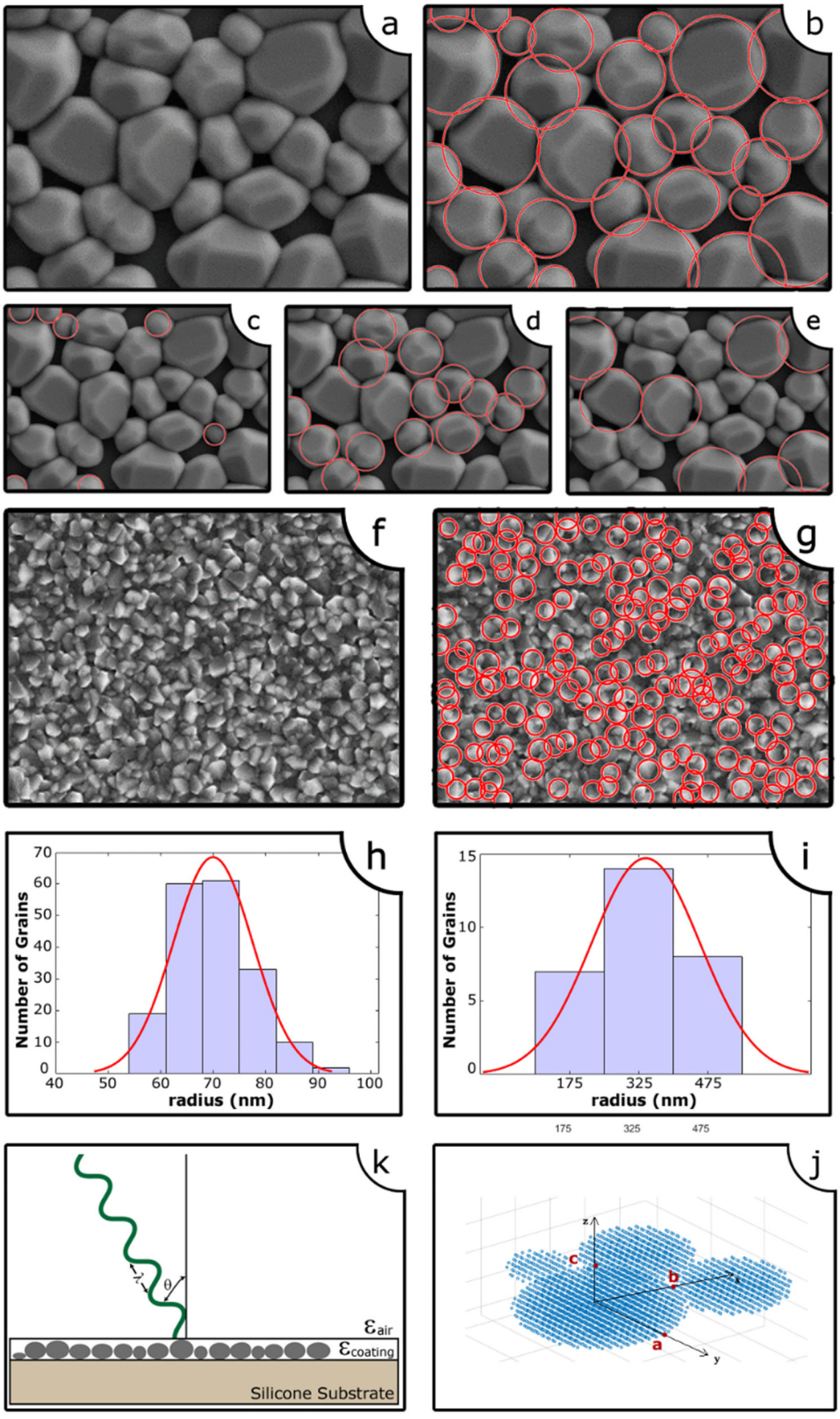

FIG. 2. A schematic description of the circular Hough Transform (CHT) based algorithm used to estimate the position in (a) large grained (f) and small grained coating. The resulting position and size is presented in (b) and (g), respectively. In order to improve the accuracy for the coating which has large grains, size domain is divided into 3 groups (e), (f), and (g), and, finally, the results are put together to estimate the final distribution in (b). The position and radius data of (b) and (g) are then used to find a histogram of the coating (i) and (h), respectively, to estimate radiative behavior of the coating. Small grained coating is estimated as an effective homogeneous medium. For the large grained coating, the shape of the grains is modeled as oblate spheroids containing 3 types of grains shown in (j). Plane wave is incident upon the coating as presented in (k).

C. Generation of the computational domain using experimental data

A schematic illustration of the samples with coarse and fine grain is given in Figs. 1(e) and 1(f), respectively. To find the particle size distribution, SEM images of the coating are used. For the specimen that was annealed at 600 °C, grains are distinguishable and have a monolayer distribution over the silicon wafer as shown in Fig. 2(a). To find the size distribution and to obtain minimum, maximum, and average grain sizes, SEM images were parameterized. Circle detection algorithms are used to obtain the size and the position data of the circle from the images. These algorithms have increased in accuracy since 1972, when Hough Transform was first outlined by Duda and Hart.[49] Briefly, a circle is parametrized by its coordinates and radius, then these are related with edge points. A decision is made by a voting procedure. In the literature, evaluations of the methods are performed on metallurgical data sets, which make the implementation of the method ideal for the type of coating in this paper. In this study, a circular Hough transform (CHT) based algorithm[49,50] is used to find the position and the radius of grains from the SEM images of the coating. Circle detection and histogram results for large grained coating are presented in Figs. 2(b) and 2(i), respectively. A periodic unit cell is used for DDA calculation, which contains two medium, one small, and one large sized grain based on the histogram data in Fig. 2(i). The resulting geometry is shown in Fig. 2(j). Considering the sizes of grains from the SEM images, the geometry of small, medium, and large particles are $a = b = 1.88c = 190$, $a = b = 2.25c = 320$, $a = b = 2.58c = 505$ nm. A simple unit that contains 2 middle, 1 small, and 1 large sized grain that is periodic from the x and y planes is constructed using dipoles. A 3032 dipole coarse version is presented in Fig. 2(j) for simplicity, which is constructed with 23 648 dipoles to satisfy accuracy criteria $2\pi|m|d/\lambda < 1$ where m is a complex refractive index of the VO_2, d is the interdipole separation distance, and λ is the wavelength in vacuum.

For the sample that is annealed at 500 °C, the particle size is small with respect to the coating annealed at 600 °C, as can be seen in Figs. 2(a) and 2(f). The average grain radius is estimated as 70 nm by CHT, and the volume fraction is taken as 0.637, which is a typical value for random closed packs. In Fig. 3, the thickness of the coating is estimated from SEM images as 350 nm.

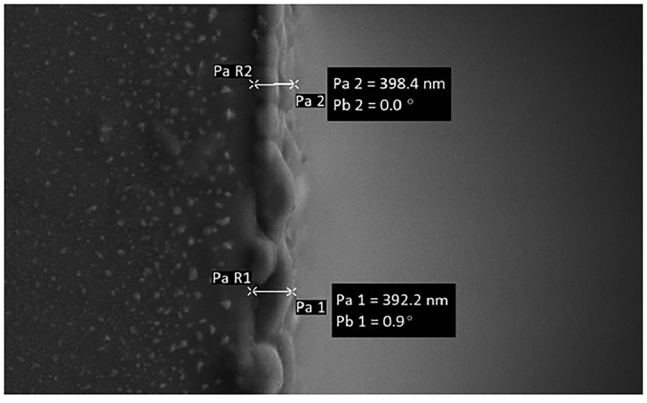

FIG. 3. Side view of the coating annealed at 600 °C. Height of the grains is taken from this image to model the coating.

III. RESULTS AND DISCUSSION

A. Morphology and composition of VO_2 nanostructured surface

We first discuss the results regarding surface morphology control through the heat treatment at different temperatures. Figure 4 shows the XRD pattern along with the surface morphology of the samples after the heat treatment at 600 °C and 500 °C. No peaks related to metallic V are observed in the XRD patterns of the as-grown V film on the Si substrate. V film is expected to be in an amorphous state when grown at room temperature prior to annealing. Heat treatment at two different temperatures results in different particle sizes, while achieving a VO_2 nanocrystal structure. It can be seen in Fig. 4(a) that XRD measurement of the sample annealed at 600 °C under Ar gas atmosphere shows the $2\theta = 27.89°$ peak associated with the (011) plane of the VO_2 monoclinic phase. After the heat treatment process of all samples, we did not observe a metallic V peak, confirming the formation of VO_2. The peak at 26.8° is due to the (110) planes of the VO_2 monoclinic phase and is not related to impurities, as reported in Ref. 51, this implies the presence of a minor volume fraction of structural variants of VO_2 due to its monoclinic state as no other oxides of V possess such a peak. The peaks at 55° and 56° belong to the (222) and the (022) planes of VO_2.[52] These peaks are almost nonexistent in the 500 °C annealed sample that could imply the tendency of VO_2 for further restructuring possibly due to thermal strain development during annealing at elevated temperatures [Fig. 4(d)]. These peaks are less significant in the 500 °C annealed sample [Fig. 4(d)]. The XRD peak in Fig. 4(a) around 44° and 64° is coming from the steel sample holder and belongs to BCC Fe, and we also noticed that its presence depends on the positioning of the samples on the stage [it is absent in the pattern in (d)]. In an attempt to distinguish the effect of annealing temperatures on peak positions, we carried out a Gaussian fit to the peaks and taking the FWHM of these, we determined the relevant positions as 27.88° and 27.89°, respectively, for the 500 °C and 600 °C annealed samples. This value is consistent with the interplanar distance of the (011) planes but is smaller than the angle resolution limit of our measurement, i.e., the step size of the scans (0.02°). This does not allow a direct comment on the few degrees reduction in the phase transition temperature of the 500 °C annealed sample with respect to the 600 °C annealed one in relation to the small 2θ shift. We also measured the XRD of the sample annealed at 400 °C. For this sample, we did not observe any monoclinic VO_2 peaks indicating that this phase could not form and was excluded from the discussions in this paper (see the supplementary material).

To bring further insight into the single phase formation of the VO_2, we also carried out Raman spectrum of the annealed samples. Figures 5(a) and 5(b) show the Raman spectrum of the sample annealed at 600 °C and 500 °C, respectively. The peak positions observed for each of the spectra marked in Fig. 5 are associated with the A_g and B_g phonon vibration modes of VO_2.[53–56]

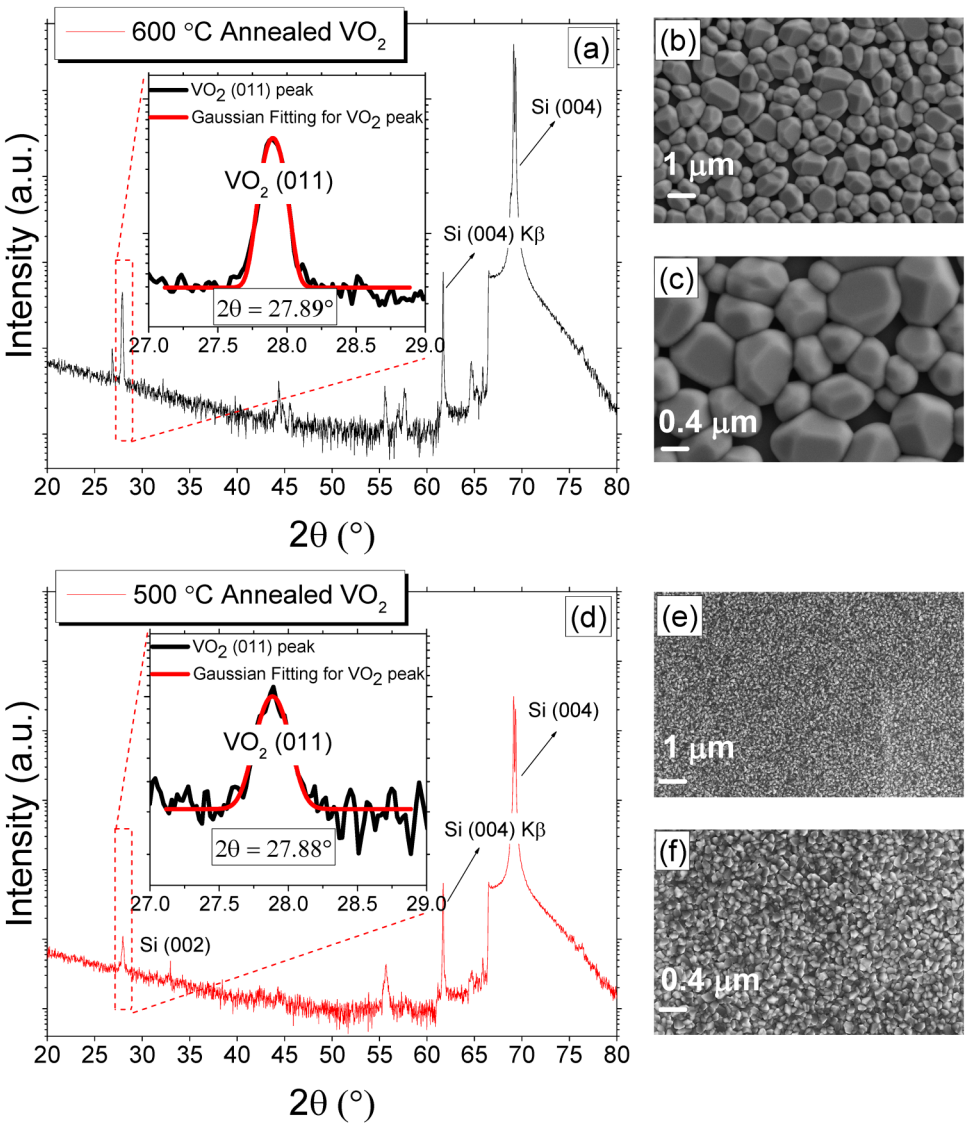

FIG. 4. θ–2θ X-ray diffraction (XRD) pattern and scanning electron microscopy (SEM) images: [(a)–(c)] at 600 °C annealed sample and [(d)–(f)] at 500 °C annealed sample.

The 192 cm^{-1}–612 cm^{-1} peaks in Fig. 5(a) and 194 cm^{-1}–613 cm^{-1} peaks in Fig. 5(b) signify the V—O bound vibrations. In addition, the rest of the peaks are assigned to the vibrational mode of the V—V and V—O bonds. The phonon modes at 612 cm^{-1} in Fig. 5(a) and 613 cm^{-1} in Fig. 5(b) are assigned to the stretching mode of the V—O vibration. The peak observed at ~140 cm^{-1} originates from an external mode, which is due to the oscillation of rigid O—V—O chains. The peak at 520 cm^{-1} is associated with the Si substrate.

To explore the possible effect of the processing temperature of VO_2 on the chemical bonding state inside the nanostructures, we carried out XPS core level spectroscopy before and after the heat treatment. The curves were deconvoluted using the Voigt curve fit. Before moving onto the discussions regarding VO_2, we first provide the XPS data of the as-grown metallic V. The deconvoluted region of the XPS spectra corresponding to the V *2p* and O *1s* peaks are due to the spin–orbit splitting for as-grown V films shown in Figs. 6(a) and 6(b). It is clearly seen that V $2p_{3/2}$ peak can be represented as a sum of 3 separate peaks at energy positions of 512.48 eV, 515.95 eV, and 517.06 eV. The lower binding energy component at 512.48 eV is attributed to a metallic V state.[57] According to the deconvolution results, the V *2p* spectrum is dominated by the peaks in the V^{4+} and V^{5+} oxidation states at 515.95 eV and 517.06 eV, respectively. The V^{4+} and V^{5+} states in addition to the O *1s* peak indicate the presence of a very thin oxide layer on the metallic V as-grown film. The metallic V peak at 512.48 eV disappears following the heat treatment of the samples whose XPS data we shall discuss below.

Figure 7 displays the V *2p* and O *1s* peaks that originate from the spin–orbit splitting for the samples annealed at 600 °C and

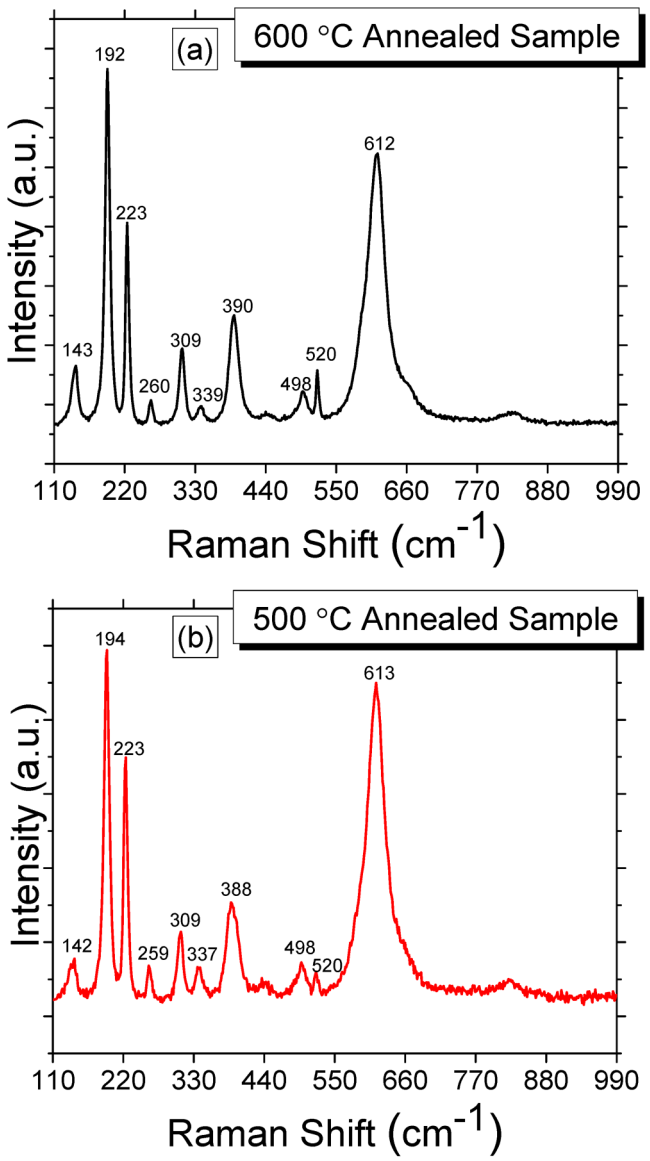

FIG. 5. Raman spectroscopy results of the as-grown V film after the heat treatment (a) at 600 °C and (b) at 500 °C.

500 °C. In Figs. 7(a) and 7(c), the V $2p_{3/2}$ spectra of the coatings exhibited two characteristic peaks at 516.39 eV and 517.77 eV for the sample annealed at 600 °C and at 516.4 eV and 517.61 eV (with the statistical deviation of ±0.25 eV) for the sample annealed at 500 °C, which correspond to the V^{4+} and V^{5+} oxidation states, respectively. In addition, there is no metallic V peak. For both two samples, O 1*s* peak at ~530 eV originates from the binding energy of the O—V bonds. The peak on the right side of O *1s* (at ~532 eV) with less intensity that is present in all our data is attributed to surface contamination mostly from C bonds [C—C, C═C, and C—(OH)].[58] Figure 7 displays the XPS spectra of the VO_2 nanostructures. The presence of the V^{5+} component in all the VO_2 samples implies an overoxidation, resulting in the formation of V_2O_5 at the surface either due to air exposure[59] or the processing temperatures. The existence of V_2O_5 at the surface has also been reported in oxides of V with high chemical purity and is easily detected by XPS measurements, since the technique is mostly sensitive to the first few atomic layers beneath the surface of the film.[60,61] Overall, the XPS results indicate that formation of the VO_2 phase is favored at higher temperatures with respect to V_2O_5 as can be deduced from the peak comparisons of V^{4+}. A curve fitting analysis to our data in Figs. 7(a) and 7(c) show that the $VO_2/VO_2 + V_2O_5$ content ratio in the sample annealed at 500 °C was 23% and this value becomes 42% for the 600 °C in addition to an increase in the nanostructure size, respectively. It must be borne in mind that XPS yields information only for the few atomic layers on the surface and is not representative of the bulk phase composition. However, the increase in the VO_2 content with increasing annealing temperature is qualitatively in agreement with XRD and Raman data. It is likely that VO_2 stabilization is assisted by temperature accompanied by grain growth in addition to the sensitivity of this system, i.e., VO_2, to oxygen partial pressure during annealing.

B. Temperature dependent spectral reflection from VO_2 thin films

In this section, we provide temperature dependent spectral ellipsometry measurements during heating for VO_2 surfaces. Figures 8(a) and 8(b) show the spectral reflection of the samples annealed at 600 °C and 500 °C, respectively. The spectral curves are obtained in the reflection mode during heating of the samples to various temperatures of 30 °C and 80 °C as indicated in Fig. 8. In Fig. 8(a), we observe that a sudden increase in the reflectance occurs around 66 °C for the sample annealed at 600 °C. An increase of the reflectance continues gradually in the IR regime as the temperature is raised as shown in Fig. 8(a). Insulator state, on the other hand, is insensitive to spectral variations of the incident radiation near the IR. The finite reflectance of the insulator phase is solely due to the difference of refractive indices at the air–sample interface.

The samples treated at 500 °C display a slightly reduced phase transition temperature and spectral reflectance than those treated at 600 °C. Figure 8(b) shows the spectral reflectance for the sample annealed at 500 °C as a function of temperature. As can be seen, the reflectance increase starts around 63 °C contrary to the coarse grained sample obtained at 600 °C displaying the jump in reflectance around 66 °C. Both samples, albeit having different IMT temperatures, display a quite sharp increase in the magnitude of reflection at their respective transition temperatures. Overall, the results in Figs. 8(a) and 8(b) clearly reveal that the IMT phase transition slightly reduces with the grain size of VO_2. The main mechanism behind this small but detectable reduction can be attributed to the relatively lower crystallinity of the 500 °C as evidenced from the (011) peak widths in Fig. 4 insets. Doping can also cause similar effects as reported in the literature.[62]

A striking observation in Fig. 8 is the impact of nanoparticle size on the spectral shape distribution, particularly near the visible regime. This raises the question as to whether such effects are due

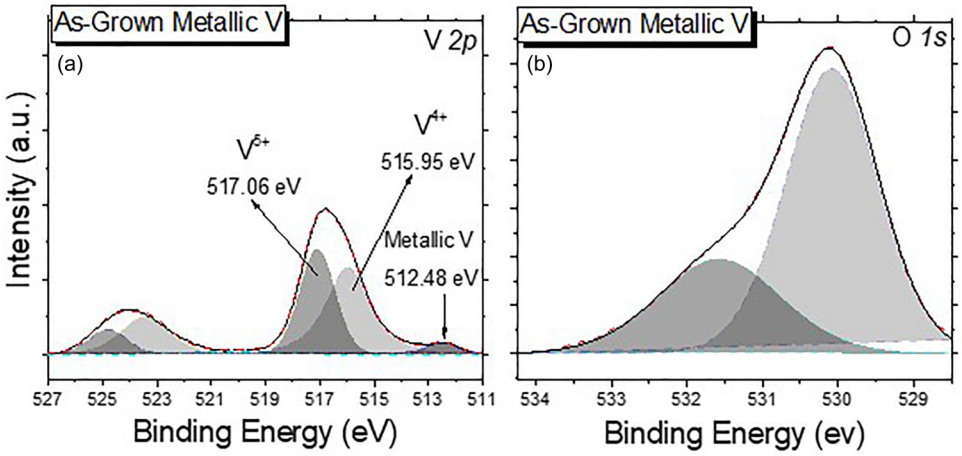

FIG. 6. (a) V *2p*, (b) O *1s* XPS spectra of the as-grown metallic V film.

to the shift in the IMT temperatures of fine and coarse grains. To highlight the difference in spectral shapes as a result of the particle size change, details of the spectral shapes for two cases are shown in the insets. In Figs. 8(b) and 8(d), the visible and near infrared parts of the spectrum are plotted for the samples annealed at 600 °C and 500 °C, respectively. Results in Fig. 8(b), which correspond to the coarse VO_2 film, reveal a weak bidirectional reflection in the visible and near infrared regions. In contrast, a more pronounced reflection is observed in the visible and near infrared regions for the fine grained sample. Especially, for the sample with finer grain size, the local spectral dip around 750 nm for the insulator state becomes a spectral peak after the transition

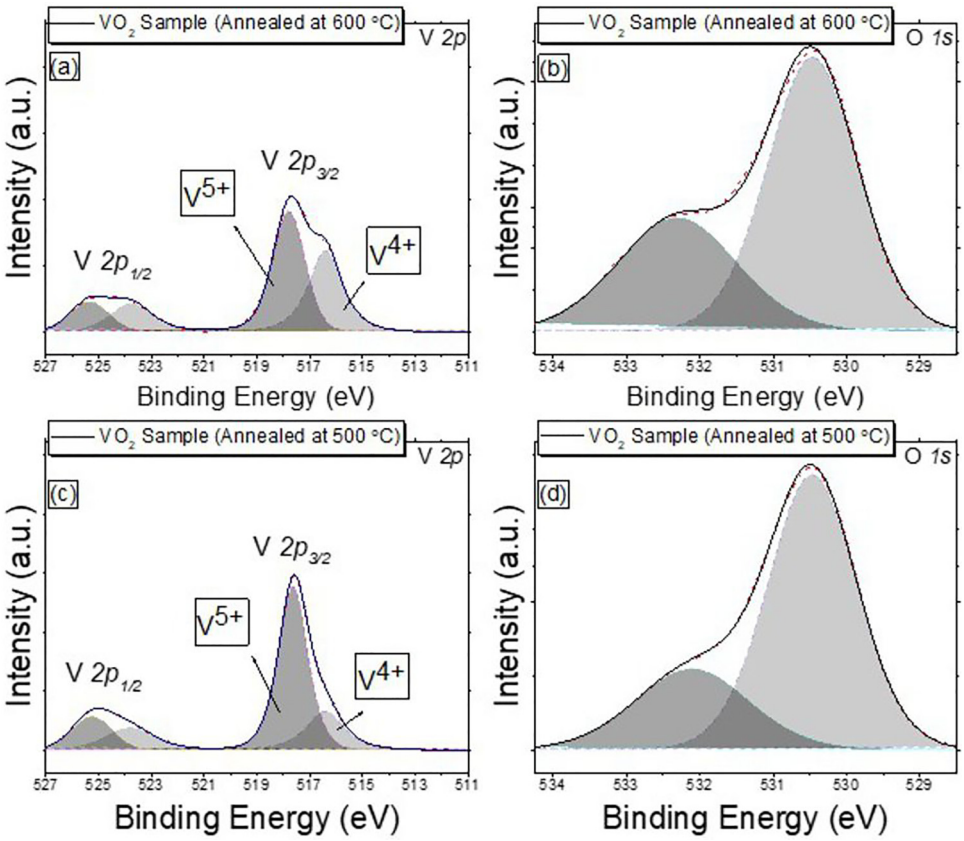

FIG. 7. (a) V *2p*, (b) O *1s* XPS spectra of the sample annealed at 600 °C and (c) V *2p*, (d) O *1s* XPS spectra of the sample annealed at 500 °C.

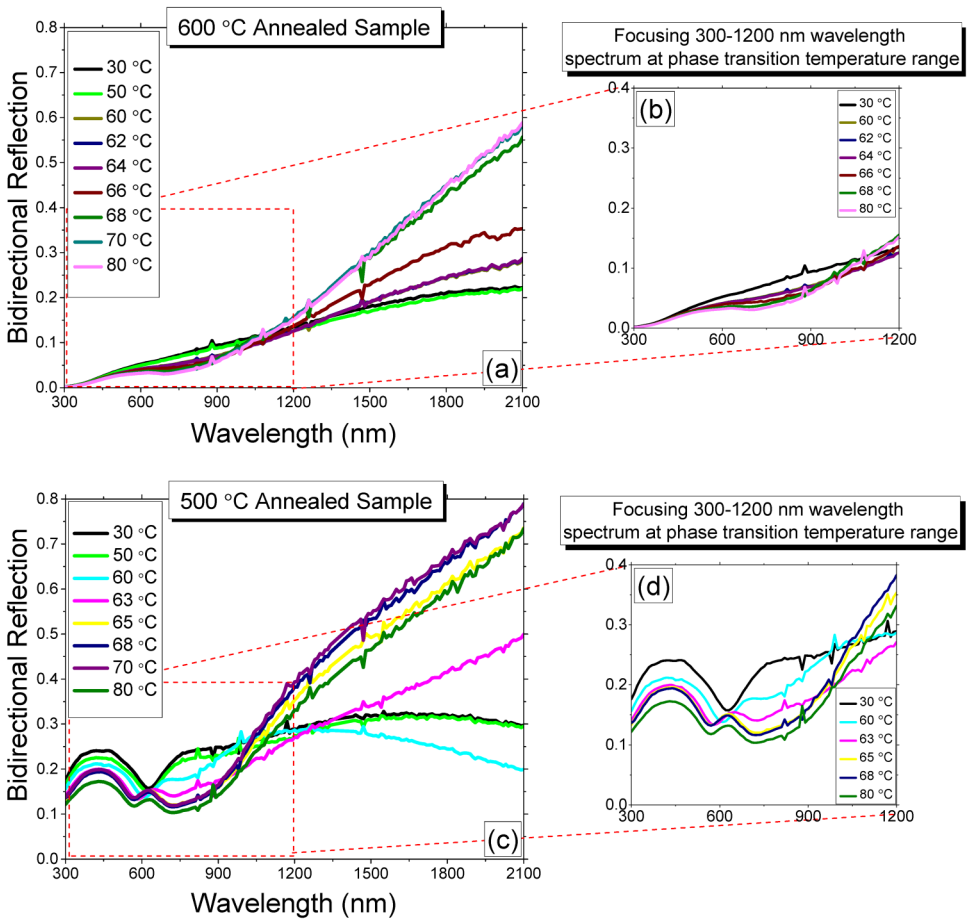

FIG. 8. Ellipsometry results of the as-grown V film after the heat treatment [(a) and (b)] at 600 °C and [(c) and (d)] at 500 °C, respectively.

temperature. The oscillatory-type of variations are more pronounced for the finer grain sized sample. To demonstrate the IMT in a clear manner, we present the 1600 nm and 1800 nm reflectance data as a function of temperature in Fig. 9 as this regime is relatively free of morphological effects. The results reveal ~3 °C difference in the IMT temperature. A slight difference in the IMT characteristics was also reported in Refs. 63 and 64, a point that must be accounted for when working with such systems using electrical resistance measurements.

To understand whether the spectral reflectance differences for the fine and coarse grained sample are due to a size effect or difference in the transition temperature, we performed numerical

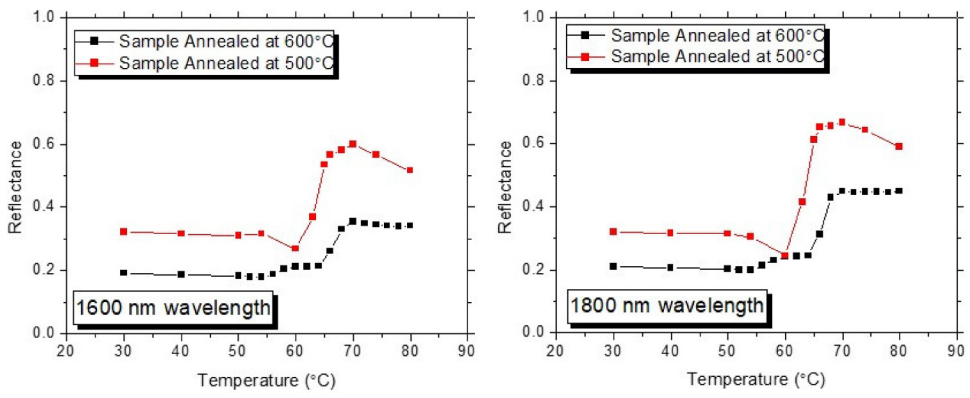

FIG. 9. Reflectance of the samples at 2 different wavelengths (1600 nm and 1800 nm) at various temperatures during heating obtained from ellipsometry experiments.

simulations as outlined in Secs. II B and C. We first provide the bidirectional reflectance of the sample annealed at 500 °C and the results are compared in Fig. 10 with the experimental measurements. Calculations show good agreement with the experimental measurements in the regime where $r/\lambda < 0.1$ is satisfied. Particles with sizes much smaller than the incident wavelength do not scatter the radiation significantly. This radiation is expected to undergo a specular reflection from the coating with a minimal diffuse reflection. Our numerical calculations confirm that the bidirectional reflectance is almost equivalent to hemispherical reflectance. Since the grains are indistinguishable compared to the incident wavelength, the surface roughness does not come into play as a parameter that would prohibit the use of effective medium theory. Therefore, reflectance is not impacted by the morphology of the fine grained surface as long as $r/\lambda < 0.1$ is satisfied. The difference between refractive indices of air and VO_2 becomes the major parameter affecting reflectance.

We next investigated the sample where the coating is annealed at 600 °C that yielded coarse grains. In Fig. 11, the bidirectional spectral reflectance measurement of the VO_2 films is compared with numerical calculations at 40 °C and 80 °C, i.e., before and after the phase change. In this case, the grain size is comparable to the wavelength. The numerical calculations indicate that, for this case, the morphology driven scattering effects are more dominant even above 68 °C and are almost insensitive to the IMT of VO_2 nanoparticles. For this sample, low bidirectional reflectance at 300 nm is observed for both states (insulator and metallic), in contrast to the sample with finer sized grains. To understand the underlying mechanism, we also investigated the total hemispherical reflectance (THR), which deviates from the bidirectional reflectance for the sample with coarse sized grains. Estimated THR along with the absorptance is presented in Fig. 12. Along with Fig. 11, Fig. 12 shows that the light is reflected diffusely at shorter wavelengths unlike the specimen annealed at 500 °C which reflects specularly at shorter wavelengths. This result confirms that the light scattering is more dominant at shorter wavelengths and leads to diffuse reflectance from the 600 °C annealed coarse grained sample. Since the r/λ ratio is larger at shorter wavelengths, particles are more distinguishable to incident radiation and therefore the light scattering is more dominant. As the wavelength gets longer, particles become less distinguishable; hence, particle scattering leading to diffuse reflectance is less dominant that results in similar reflectance for specimens

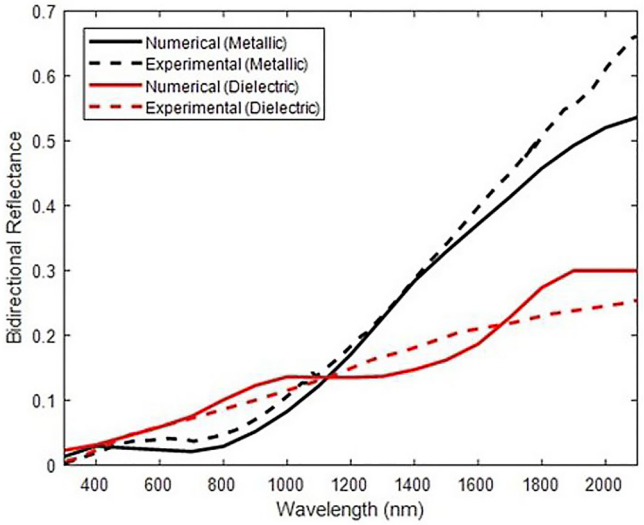

FIG. 11. Simulated bidirectional reflectance for the sample annealed at 600 °C.

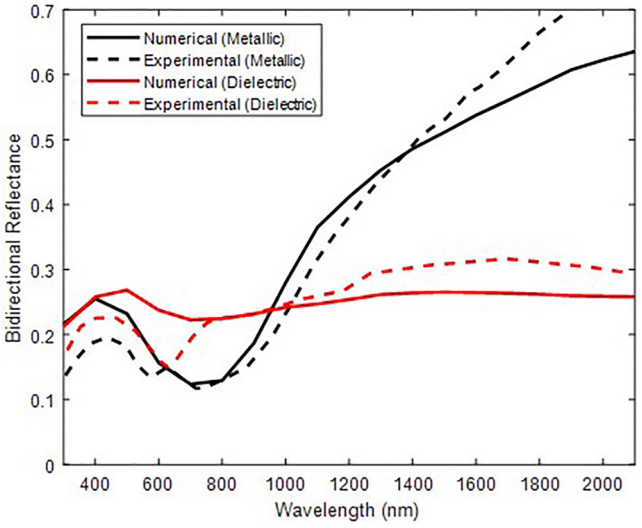

FIG. 10. Simulated bidirectional reflectance for the sample annealed at 500 °C. Reflectance shown here are for 68 °C (metallic state) and 50 °C (insulator state).

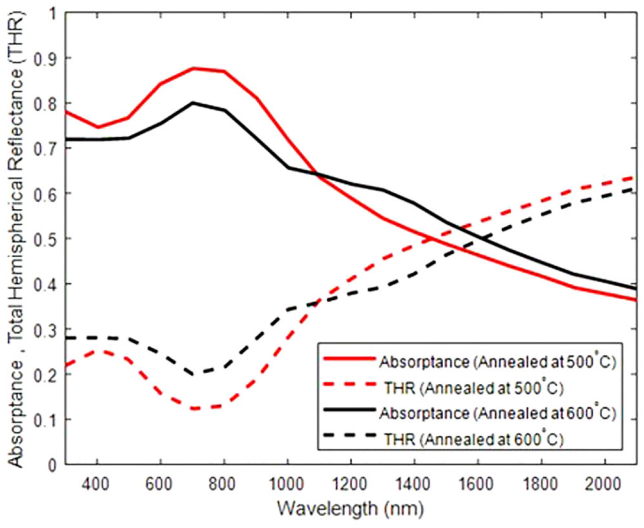

FIG. 12. Simulated absorptance and total hemispherical reflectance for the specimen annealed at 500 °C and 600 °C.

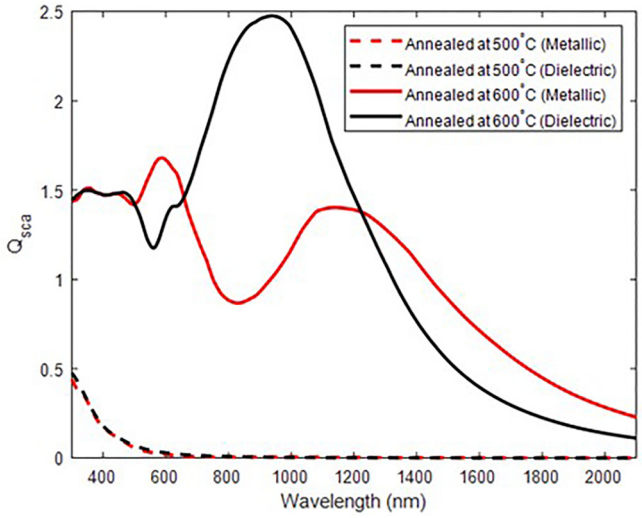

FIG. 13. Simulated scattering efficiencies of nanostructures annealed at 500 °C and 600 °C which have grain sizes of 70 nm and 330 nm, respectively.

annealed at different temperatures of 500 °C and 600 °C. No significant change is observed in absorptance for samples annealed at different temperatures. Our results indicate that the main mechanism leading to different spectral line shapes is the morphological differences leading to diffuse and spectral reflectance.

To further emphasize the temperature and morphology dependence of the reflectance in different samples, spectral scattering efficiencies of spherical particles at different sizes (70 nm for 500 °C and 330 nm for 600 °C) are calculated using the Mie theory. The results are presented in Fig. 13 showing that the scattering behavior of the specimen at 600 °C dominates at shorter wavelengths. At longer wavelengths, morphology related scattering effects vanish for both specimens, and their spectral reflections tend to converge to a single curve both in the insulator and metallic states of VO_2. Thus, the transition dependent variations in reflectance, i.e., the intrinsic VO_2 related effects for the 500 °C and 600 °C annealed samples become comparable only at longer wavelengths where scattering effects are negligible for both morphologies.

IV. CONCLUSIONS

In summary, we demonstrated that the optical response of VO_2 thin films is sensitive to changes in the grain size through morphology. While IMT is the major factor determining the reflectance for the near-IR spectrum, the optical response of the samples in the near-visible spectrum is governed by the morphology of VO_2. The fine and coarse grained VO_2 thin films in this work display dramatically different bidirectional spectral reflectance particularly in the visible regime. Our results indicate that the main mechanism leading to different spectral line shapes stems from the morphological differences leading to diffuse and specular reflectance from the coarse grained samples. For the coarse grained samples, the light scattering is more dominant at shorter wavelengths and leads to diffuse reflectance from the sample, since r/λ ratio is larger at shorter wavelengths. For the fine grained samples, the sample–air interface behaves as a more homogenous bilayer, resembling a filmlike response, leading to bidirectional reflectance demonstrated by the EMT calculations. The scattering simulations were vital in distinguishing morphological effects from those one would expect to emanate from the intrinsic material property related effects, a point that can easily be overlooked when interpreting the IMT transition from optical experiments. These simulations also highlight the morphology-driven transition from specular to diffuse spectral reflection as the size of nanostructures increases.

SUPPLEMENTARY MATERIAL

See the supplementary material for the XRD pattern of the VO_2 thin films annealed at 400 °C following e-beam growth of metallic V on the (001) Si substrate.

ACKNOWLEDGMENTS

This work was supported by TUBITAK through Project No. 115M033.

REFERENCES

[1]H.-T. Kim, B.-G. Chae, D.-H. Youn, S.-L. Maeng, G. Kim, K.-Y. Kang, and Y.-S. Lim, New J. Phys. **6**, 52 (2004).
[2]Z. Tao, F. Zhou, T.-R. T. Han, D. Torres, T. Wang, N. Sepulveda, K. Chang, M. Young, R. R. Lunt, and C.-Y. Ruan, Sci. Rep. **6**, 38514 (2016).
[3]H. Yoon, M. Choi, T.-W. Lim, H. Kwon, K. Ihm, J. K. Kim, S.-Y. Choi, and J. Son, Nat. Mater. **15**, 1113 (2016).
[4]S. Wang, L. Kang, and D. H. Werner, Sci. Rep. **7**, 4326 (2017).
[5]F. Morin, Phys. Rev. Lett. **3**, 34 (1959).
[6]M. Marezio, D. B. McWhan, J. Remeika, and P. Dernier, Phys. Rev. B **5**, 2541 (1972).
[7]T.-H. Yang, S. Nori, H. Zhou, and J. Narayan, Appl. Phys. Lett. **95**, 102506 (2009).
[8]H. Zhou, M. F. Chisholm, T.-H. Yang, S. J. Pennycook, and J. Narayan, J. Appl. Phys. **110**, 073515 (2011).
[9]J. Montero, Y.-X. Ji, S.-Y. Li, G. A. Niklasson, and C. G. Granqvist, J. Vac. Sci. Technol. B **33**, 031805 (2015).
[10]P. Jin, K. Yoshimura, and S. Tanemura, J. Vac. Sci. Technol. A **15**, 1113 (1997).
[11]Y. Luo, S. Pan, S. Xu, L. Zhong, H. Wang, and G. Li, J. Alloys Compd. **664**, 626 (2016).
[12]M. Taha, S. Walia, T. Ahmed, D. Headland, W. Withayachumnankul, S. Sriram, and M. Bhaskaran, Sci. Rep. **7**, 17899 (2017).
[13]M. Yang, Y. Yang, B. Hong, L. Wang, K. Hu, Y. Dong, H. Xu, H. Huang, J. Zhao, and H. Chen, Sci. Rep. **6**, 23119 (2016).
[14]L. Fan, S. Chen, Y. Wu, F. Chen, W. Chu, X. Chen, C. Zou, and Z. Wu, Appl. Phys. Lett. **103**, 131914 (2013).
[15]J. Leroy, A. Bessaudou, F. Cosset, and A. Crunteanu, Thin Solid Films **520**, 4823 (2012).
[16]V. Théry, A. Boulle, A. Crunteanu, J.-C. Orlianges, A. Beaumont, R. Mayet, A. Mennai, F. Cosset, A. Bessaudou, and M. Fabert, J. Appl. Phys. **121**, 055303 (2017).
[17]R. Marvel, K. Appavoo, B. Choi, J. Nag, and R. Haglund, Appl. Phys. A **111**, 975 (2013).
[18]L. Kang, Y. Gao, and H. Luo, ACS Appl. Mater. Interfaces **1**, 2211 (2009).
[19]Y. Cui and S. Ramanathan, J. Vac. Sci. Technol. A **29**, 041502 (2011).
[20]Z. Liu, B. Banar, S. Butun, H. Kocer, K. Wang, J. Scheuer, J. Wu, and K. Aydin, Opt. Mater. Express **8**, 2151 (2018).

[21]M. J. Dicken, K. Aydin, I. M. Pryce, L. A. Sweatlock, E. M. Boyd, S. Walavalkar, J. Ma, and H. A. Atwater, Opt. Express **17**, 18330 (2009).
[22]L. Fan, Y. Chen, Q. Liu, S. Chen, L. Zhu, Q. Meng, B. Wang, Q. Zhang, H. Ren, and C. Zou, ACS Appl. Mater. Interfaces **8**, 32971 (2016).
[23]S. Lysenko, A. Rua, V. Vikhnin, J. Jimenez, F. Fernandez, and H. Liu, Appl. Surf. Sci. **252**, 5512 (2006).
[24]S. Cueff, D. Li, Y. Zhou, F. J. Wong, J. A. Kurvits, S. Ramanathan, and R. Zia, Nat. Commun. **6**, 8636 (2015).
[25]A. Joushaghani, J. Jeong, S. Paradis, D. Alain, J. S. Aitchison, and J. K. Poon, "Characteristics of the current-controlled phase transition of VO_2 microwires for hybrid optoelectronic devices," Photonics **2**, 916 (2015).
[26]E. Rahimi and K. Şendur, Nanophotonics **7**, 659 (2018).
[27]E. Strelcov, Y. Lilach, and A. Kolmakov, Nano Lett. **9**, 2322 (2009).
[28]K.-E. Peiponen, A. Zeitler, and M. Kuwata-Gonokami, *Terahertz Spectroscopy and Imaging* (Springer, 2012), Vol. 171.
[29]Y. Yang, S. Basu, and L. Wang, J. Quant. Spectrosc. Radiat. Transf. **158**, 69 (2015).
[30]H. S. Choe, J. Suh, C. Ko, K. Dong, S. Lee, J. Park, Y. Lee, K. Wang, and J. Wu, Sci. Rep. **7**, 7131 (2017).
[31]J. Mizsei and J. Lappalainen, Procedia Eng. **168**, 1070 (2016).
[32]A. Hendaoui, N. Émond, S. Dorval, M. Chaker, and E. Haddad, Sol. Energy Mater. Sol. Cells **117**, 494 (2013).
[33]M. Wang, Y. Xue, Z. Cui, and R. Zhang, J. Phys. Chem. C **122**, 8621 (2018).
[34]M. Wang, Z. Cui, Y. Xue, and R. Zhang, Cryst. Growth Des. **18**, 4220 (2018).
[35]R. Lopez, T. Haynes, L. A. Boatner, L. Feldman, and R. Haglund, Opt. Lett. **27**, 1327 (2002).
[36]E. Donev, J. Ziegler, R. Haglund, Jr., and L. Feldman, J. Opt. A **11**, 125002 (2009).
[37]R. Lopez, T. Haynes, L. Boatner, L. Feldman, and R. Haglund, Jr., Phys. Rev. B **65**, 224113 (2002).
[38]R. Lopez, L. C. Feldman, and R. F. Haglund, Jr., Phys. Rev. Lett. **93**, 177403 (2004).
[39]S. Lysenko, V. Vikhnin, A. Rua, F. Fernandez, and H. Liu, Phys. Procedia **13**, 18 (2011).
[40]M. E. Uslu, I. B. Misirlioglu, and K. Sendur, Opt. Mater. Express **8**, 2035 (2018).
[41]K. Laaksonen, S.-Y. Li, S. Puisto, N. Rostedt, T. Ala-Nissila, C.-G. Granqvist, R. Nieminen, and G. A. Niklasson, Sol. Energy Mater. Sol. Cells **130**, 132 (2014).
[42]L. E. Nielsen, J. Phys. D **7**, 1549 (1974).
[43]D. W. Mackowski, J. Quant. Spectrosc. Radiat. Transf. **189**, 361 (2017).
[44]E. M. Purcell and C. R. Pennypacker, Astrophys. J. **186**, 705 (1973).
[45]B. T. Draine, Astrophys. J. **333**, 848 (1988).
[46]B. T. Draine and P. J. Flatau, J. Opt. Soc. Am. A **25**, 2693 (2008).
[47]A. Penttilä, E. Zubko, K. Lumme, K. Muinonen, M. A. Yurkin, B. Draine, J. Rahola, A. G. Hoekstra, and Y. Shkuratov, J. Quant. Spectrosc. Radiat. Transf. **106**, 417 (2007).
[48]M. Currie, M. A. Mastro, and V. D. Wheeler, Opt. Mater. Express **7**, 1697 (2017).
[49]R. O. Duda and P. E. Hart, Commun. ACM **15**, 11 (1972).
[50]T. J. Atherton and D. J. Kerbyson, Image Vis. Comput. **17**, 795 (1999).
[51]H. J. Song, M. Choi, J.-C. Kim, S. Park, C. W. Lee, S.-H. Hong, B.-K. Kim, and D.-W. Kim, Sci. Rep. **6**, 30202 (2016).
[52]C. Wu, X. Zhang, J. Dai, J. Yang, Z. Wu, S. Wei, and Y. Xie, J. Mater. Chem. **21**, 4509 (2011).
[53]A. Cavalleri, T. Dekorsy, H. H. Chong, J.-C. Kieffer, and R. W. Schoenlein, Phys. Rev. B **70**, 161102 (2004).
[54]X. Yuan, W. Zhang, and P. Zhang, Phys. Rev. B **88**, 035119 (2013).
[55]G. Petrov, V. Yakovlev, and J. Squier, Appl. Phys. Lett. **81**, 1023 (2002).
[56]P. Schilbe, Physica B **316**, 600 (2002).
[57]C. Blaauw, F. Leenhouts, F. van der Woude, and G. Sawatzky, J. Phys. C **8**, 459 (1975).
[58]F. Ureña-Begara, A. Crunteanu, and J.-P. Raskin, Appl. Surf. Sci. **403**, 717 (2017).
[59]M. J. Powell, I. J. Godfrey, R. Quesada-Cabrera, D. Malarde, D. Teixeira, H. Emerich, R. G. Palgrave, C. J. Carmalt, I. P. Parkin, and G. Sankar, J. Phys. Chem. C **121**, 20345 (2017).
[60]E. Hryha, E. Rutqvist, and L. Nyborg, Surf. Interface Anal. **44**, 1022 (2012).
[61]K. A. Wepasnick, B. A. Smith, J. L. Bitter, and D. H. Fairbrother, Anal. Bioanal. Chem. **396**, 1003 (2010).
[62]X. Tan, T. Yao, R. Long, Z. Sun, Y. Feng, H. Cheng, X. Yuan, W. Zhang, Q. Liu, and C. Wu, Sci. Rep. **2**, 466 (2012).
[63]L. Wang, I. Novikova, J. M. Klopf, S. Madaras, G. P. Williams, E. Madaras, J. Lu, S. A. Wolf, and R. A. Lukaszew, Adv. Opt. Mater. **2**, 30 (2014).
[64]S. Kumar, J. P. Strachan, A. D. Kilcoyne, T. Tyliszczak, M. D. Pickett, C. Santori, G. Gibson, and R. S. Williams, Appl. Phys. Lett. **108**, 073102 (2016).